Front. Earth Sci. 2022, 16(3): 696–710
https://doi.org/10.1007/s11707-022-1020-3

RESEARCH ARTICLE

Geophysical characteristics of anthracites with various structures: a case study on the southern Qinshui Basin, north China

Juan TENG[1,2], Zhigang WEN (✉)[1,2], Chen LI[3], Lingye MENG[4]

1 Hubei Key Laboratory of Petroleum Geochemistry and Environment, Yangtze University, Wuhan 430100, China
2 College of Resources and Environment, Yangtze University, Wuhan 430100, China
3 Research Institute Company Limited, CNOOC, Beijing 100028, China
4 Institute of Petroleum Exploration and Development of PetroChina Tarim Oilfield, Korla 841000, China

Abstract Deformation of coals under tectonic movements could cause reduction of mechanical strength and enhancement of gas adsorption, which might result in coal and gas outburst, and cause safety and environmental issues. In this study, geophysical characteristics of coals with various structures were investigated with a special emphasis on characterization of pore size distribution, rock mechanical strength, acoustic emission, resistivity and acoustic velocity of anthracites with three types of structures in the Qinshui Basin, north China. The studied No. 3 coal seam developed three types of structures, namely undeformed coal, cataclastic coal, and granular coal. Petrographic observations under scanning electron microscope and pore size distribution using N_2 and CO_2 adsorption of anthracites of three types show that the undeformed coal consists of primary micropores, and cataclastic coal is mainly composed of mesopores and well-connected fractures. In comparison, granular coal has the least mesopores. Rock mechanical strength, acoustic emission, resistivity and acoustic velocity of coals with three structure types were investigated under uniaxial and triaxial compression. With increasing degree of deformation of anthracites, compression strength, Young's modulus, density, acoustic emission counting and acoustic velocity decreases, while resistivity increases. We suggest that the evolution of pore size distribution of anthracites with increasing degree of deformation contributed to variations of geophysical characteristics of coals with different structures to some extent.

Keywords geophysical characteristics, coal structures, pore size distribution, acoustic emission, electrical resistivity, acoustic velocity

Received March 24, 2022; accepted June 13, 2022

E-mail: wzg728@sina.com

1 Introduction

Intense deformation of coalbeds might lead to coal and gas outburst (Sobczyk, 2011; Yin et al., 2016; Nie et al., 2019; Ma et al., 2020), due to changes of geophysical and chemical characteristics during coal deformation (Song, 2012; Chen et al., 2017; Li et al., 2021a; Yu et al., 2020b). According to the degree of tectonic deformation, coals were classified into different types of structures (Fu et al., 2009; Jiang et al., 2010; Li et al., 2011; Xue et al., 2012; Teng et al., 2015; Yao et al., 2016). At the beginning of the 20th century, based on the macroscopic observation and characteristics of joints and fissures and fracture morphology, coal structure were divided into five types: non-destructive coal, destructive coal, strongly destructive coal, pulverized coal and fully pulverized coal. Qu et al. (2010) divided coal structure into seven types: primary cataclastic coal, massive cataclastic coal, flake cataclastic coal, fragmentary coal, scale coal, crumpled coal and crumpled mylonite coal. In general, many classification methods have been proposed, and four types of coal structure, namely undeformed, cataclastic, granular and mylonite coal, have been widely used (Teng et al., 2015). Undeformed coals commonly have intact and massive coal structure, cataclastic coals are easily broken into large fragments with interconnected exogenous fractures, and granulated coals are easily broken into small fragments and even powders (Teng et al., 2015).

Physical characteristics of coal reservoirs change during coal deformation. Cataclastic coal develops well-connected fractures (Teng et al., 2015), while mylonite coal has very low connection, not conductive for coalbed

methane development and coal mine safety (Sobczyk, 2011; Godyń, 2016). Deformation of coals promotes macromolecular chain breaking, functional groups falling off, and unpaired electron bonding and aromatization of middle molecular structures (Qu et al., 2010). X-ray diffraction results show that the macromolecular structure of deformed coals has relatively low stability (Li et al., 2013). Deformed coals exhibit desorption hysteresis phenomenon, and changes of pore size distribution and conversion of adsorption potential energy are the causes for the adsorption increases of deformed coals (Chen et al., 2010). Pore size distribution of coals with various structures shows significant differences (Zhang et al., 2008; Skoczylas et al., 2014; Li et al., 2015b; Zhou et al., 2016). Rock mechanical characteristics of coals with various structures under triaxial compression were conducted, and the results show that from undeformed to granular coal, compressive strength decreases (Bieniawski, 1968; Frodsham and Gayer, 1999; Deisman et al., 2010; Cheng and Pan, 2020; Guo et al., 2021), and compressive strength, Young's modulus and maximum strain of methane-bearing deformed coal increase with increasing confining pressure (Li et al., 2010). Despite abundant information on geophysical characteristics of coal deformation, much less is known about how coal deformation controls its geophysical characteristics.

The Qinshui Basin is one of the largest coalbed methane (CBM) production areas in China, with annual CBM production more than 1 billion cubic meters (Tao et al., 2019; Wu et al., 2020; Chen et al., 2021). Coalbeds in the Qinshui Basin, underwent multistage tectonic movements (Li et al., 2018; Wang et al., 2018; Zhang et al., 2019; Yu et al., 2020a), and coal bed has relatively low compressive strength, which results in brittle or ductile deformation of coal reservoirs (Liu et al., 2018; Xie et al., 2019; Li et al., 2021b). In the Qinshui Basin, coal structure underwent relatively minor tectonic movement, and mylonite coal was not developed in this area. Therefore, based on the degree of deformation of coals, coal structure types are composed of undeformed coal, cataclastic coal and granular coal (Teng et al., 2015). This study investigates porosity characteristics, rock mechanical characteristics, acoustic emission (AE), resistivity and acoustic velocity in three structure types of anthracites in the Qinshui Basin. The same coalification history of these three types of coal structures eliminates the differences in geophysical characteristics due to coalification. Our main objective is to document the range of variations in geophysical characteristics of three types of coal structures to understand how and why these structure types can make a difference. To address these issues, microscopic observations, porosimetry, rock mechanical characteristics, AE, resistivity and acoustic velocity were documented and compared among the studied three types of coal structures.

2 Geological setting

The Qinshui Basin is located in the south-east of Shanxi Province, covering an area of 23.5 × 10^3 km^2 (Fig. 1), which is the most important coal and coalbed methane mining area in China, and the commercial production of coalbed methane is considerable (Su et al., 2005; Cai et al., 2011; Lv et al., 2012; Liu et al., 2014; Xu et al., 2014). The Qinshui Basin, evolved from the late Paleozoic basement to the end of Mesozoic, and coalification and thermogenic gas generation were affected by tectonic thermal events in the basin during the Yanshan orogenic movement from Jurassic to Cretaceous, resulting in high thermal maturity and vitrinite reflectance of 2.2%–4.5% (Su et al., 2005; Lv et al., 2012). The study area, located in the southern section of the Qinshui synclinal basin, with the south-east boundary of the Sidou fault and the north and west open boundaries, is gentle and broad, with a small dip angle, usually 2°–7°, and an average of 4° (Teng et al., 2015). Structures in the study area are relatively simple, with few large faults, mainly secondary folds and small faults, resulting in that coal beds in this area experienced multi-stage tectonic movements (Su et al., 2005; Cai et al., 2011; Li et al., 2011; Tao et al., 2012).

The southern Qinshui Basin is mainly composed of carboniferous Benxi and Taiyuan Formations, Permian Shanxi, Shihezi and Shiqianfeng Formations, and Triassic

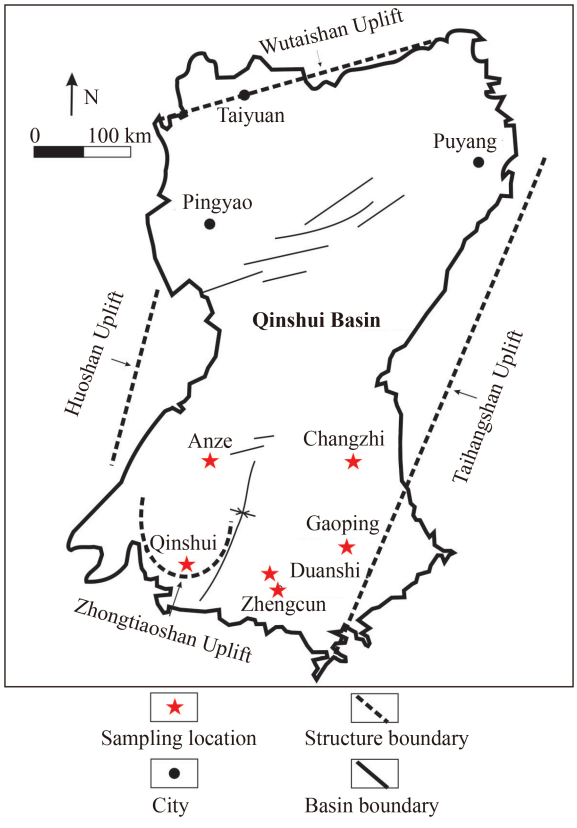

Fig. 1 Sampling locations in southern Qinshui Basin.

and Quaternary sediments (Wei et al., 2007; Lv et al., 2012; Tao et al., 2012), of which No. 3 coal seam of Lower Permian Shanxi Formation and No. 15 coal seam of Upper Carboniferous Taiyuan Formation are the main coal-bearing seams. The No. 3 coal seam, deposited in delta plain environment, with a thickness of 3–7 m, underwent plutonic metamorphism at the end of Triassic, and metamorphism degree increased due to tectonic thermal events, resulting in the formation of peranthracites. The No. 3 coal seam with relatively shallow burial depth of about 600–1200 m was investigated in this study (Jin et al., 2011; Zou et al., 2013).

3 Samples and analytical methods

3.1 Samples

Ten fresh outcrop samples were collected from 9 coal mine locations of southern Qinshui Basin, north China. The samples were well preserved in plastic bags immediately after collection. The sampling locations are shown in Fig. 1.

3.2 Proximate analysis and petrographic observations

Proximate analysis was followed China national standard GB212–77. Petrographic analysis of anthracite with various textures were examined using a field-emission scanning electron microscope (SEM) in low vacuum mode. The accelerating voltage was 20 kV and working distance was about 25 mm. For organic petrographic analysis, sample preparation followed standard organic petrography procedures (ICCP, 1963). Maximum vitrinite reflectance ($R_{o,max}$) and maceral composition were determined using microscope in reflected light, oil immersion.

3.3 Porosimetry

In this study, pores are classified into micropores (diameter <2 nm), mesopores (2–50 nm), and macropores (diameter >50 nm), which follows that of the International Union of Pure and Applied Chemistry (Orr, 1977). Samples of ~60 mesh (~250 μm) in size and weighing 1.5 to 2 g were analyzed with nitrogen (N_2) adsorption to evaluate mesopore characteristics, and carbon dioxide (CO_2) adsorption to analyze micropore size distribution, using Micromeritics ASAP–2020 apparatus. Coal texture samples were degassed at about 110°C in a vacuum for about 24 h to remove adsorbed moisture and volatile matter before gas adsorption. N_2 adsorption were operated at the temperature of 77.35 K, and both adsorption and desorption analyses were conducted to determine mesopore surface areas and volumes, which were calculated according to the adsorption theories of Brunauer-Emmett-Teller (BET) and Barrett-Joyner-Halenda (BJH). For CO_2 adsorption, coal texture samples were conducted at temperature of 273.1 K, and micropore size information were calculated using Dubinin-Radushkevich (D-R) and Dubinin-Astakhov (D-A) methods (Webb and Orr, 1997; Clarkson and Bustin, 1999; Mastalerz et al., 2012, 2013; Liu et al., 2021).

3.4 Acoustic emission and electrical resistivity analysis under uniaxial compression

Anthracites used for compression tests were drilled from fresh block samples, which were conducted at China United Coalbed Methane National Engineering Research Center. Drilled samples have a diameter of 2.5 cm and height of 5.0 cm. Because cataclastic and granular coals are fragile and easy to break, drilling processes were conducted very slowly and carefully, usually taking about 4 to 5 h each sample.

Uniaxial compression tests were conducted at Coal and Rock Dynamic Disaster Simulation Laboratory, China University of Mining and Technology. The uniaxial compression tests of anthracite with various textures were carried out using servo testing machine MTS815.2, which automatically recorded the load and displacement during compression. The testing system consists of loading system, servo test system, and data collection system (Fig. 2). Stress loading rate is 10 N/s. The maximum load is up to 250 kN, which exceeds the compression failure requirements of coals. The AE sensor with a frequency of 47.85 kHz, was glued to the surface of the cylindrical samples (diameter 2.5 cm) with Vaseline and secured with conductive tape. The AE sensor frequency used in this paper is 47.85 kHz. For electrical resistivity tests, the resistivity sensors were secured to the top and bottom of the cylindrical samples, and an inductance capacitance resistance (LCR) meter (100 Hz–100 kHz) was used for resistivity records. The LCR meter needs to be preheated before compression tests. Two sets of uniaxial compression tests were conducted in this study, with one set of samples air-dried and the other set of samples water-saturated for at least 24 h before analysis.

3.5 Acoustic velocity analysis under triaxial compression

Triaxial compression experiments were conducted at Mechanics Laboratory, China University of Petroleum. The loading system is GCTS high-temperature and high-pressure rock triaxial apparatus. The maximum axial pressure is 1500 kN, and the axial loading frequency is 10 Hz. The acoustic wave tester used in this study is tested based on the ultrasonic pulse penetration method. Before the test, the plexiglass standard sample is used to calibrate the acoustic wave test system to ensure the stability of the transmitted signal. The data collection system automatically recorded the AE time t_0 and the

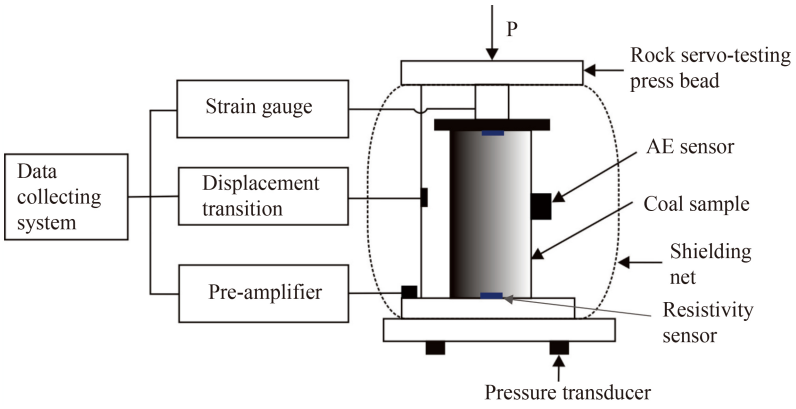

Fig. 2 Acoustic emission (AE) and resistivity testing system of coal structures under uniaxial compression.

acoustic receiving time t_1 of the receiving probe, and the p wave velocity of the sample was calculated using the following equation: $v_P = L/\Delta t$, where v_P is the P wave velocity (m/s), L is the sample length (m), t is the time difference (s). S wave velocity is not affected by sample size. More information of triaxial compression could be found in (Geng et al., 2016). Three structures types of anthracite sample in cylinder with a diameter of 2.5 cm and height of 5.0 cm were used for velocity analysis under triaxial compression.

4 Results

4.1 Proximate analysis and maceral composition

Ten anthracite samples with various coal textures were collected for proximate analysis (Table 1) and microscopic observations (Figs. 3–5). Undeformed coal samples have medium moisture and ash content, the highest volatile component and the lowest fixed carbon content. In comparison, cataclastic coal samples have the largest moisture and fixed carbon content and the lowest ash and volatile content. Granular coal samples have the lowest moisture content, the highest ash content, and medium volatile and fixed carbon content.

Three coal samples with different textures were selected for microscopic observations (Table 2). In this paper, anthracites are high grade coals, which has obvious optical anisotropy. Thus, maximum of vitrinite reflectance ($R_{o,max}$) were used to evaluate thermal maturation of anthracites instead of average value of vitrinite reflectance. Three anthracites with different structures are in over-mature stage with $R_{o,max}$ of 2.28% to 3.84%. Maceral composition results show all anthracite samples are dominated by the vitrinite group with a content higher than 70 vol%, and the inertinite group content ranges from 6.6% to 28.2 vol%. No liptinite group macerals were observed in the studied anthracite samples, and mineral matter is no higher than 1.4 vol%.

Table 1 Sampling locations and proximate analysis of three types of coal textures

Coal structure	Sample	Coal mine	M_{ad}/%	A_d/%	V_{daf}/%	FC_d/%
Undeformed coal	U1	Qinshui Qudi	1.28	14.51	10.37	89.63
	U2	Qinshui Qudi	1.22	16.41	10.68	89.32
	U3	Anze Yuhetai	0.73	13.27	19.72	80.28
	U4	Changzhi Changcun	1.20	9.27	25.77	74.23
		Average	**1.11**	**13.37**	**16.64**	**83.37**
Cataclastic coal	C1	Changzhi Yuwu	0.85	8.33	15.72	84.28
	C2	Qinshui Guohua	1.59	8.13	8.54	91.46
	C3	Qinshui Duanshi	1.91	10.23	9.32	90.68
	C4	Qinshui Sihe	2.13	13.59	13.34	86.66
		Average	**1.62**	**10.07**	**11.73**	**88.27**
Granular coal	G1	Gaoping Shenjiazhuang	0.84	23.93	15.13	84.87
	G2	Gaoping Niushan	1.45	8.14	13.54	86.46
		Average	**1.15**	**16.04**	**14.34**	**85.67**

Notes: M, moisture; A_d, Ash yield on dry basis; V_{daf}, volatile matter on dry and ash-free basis.

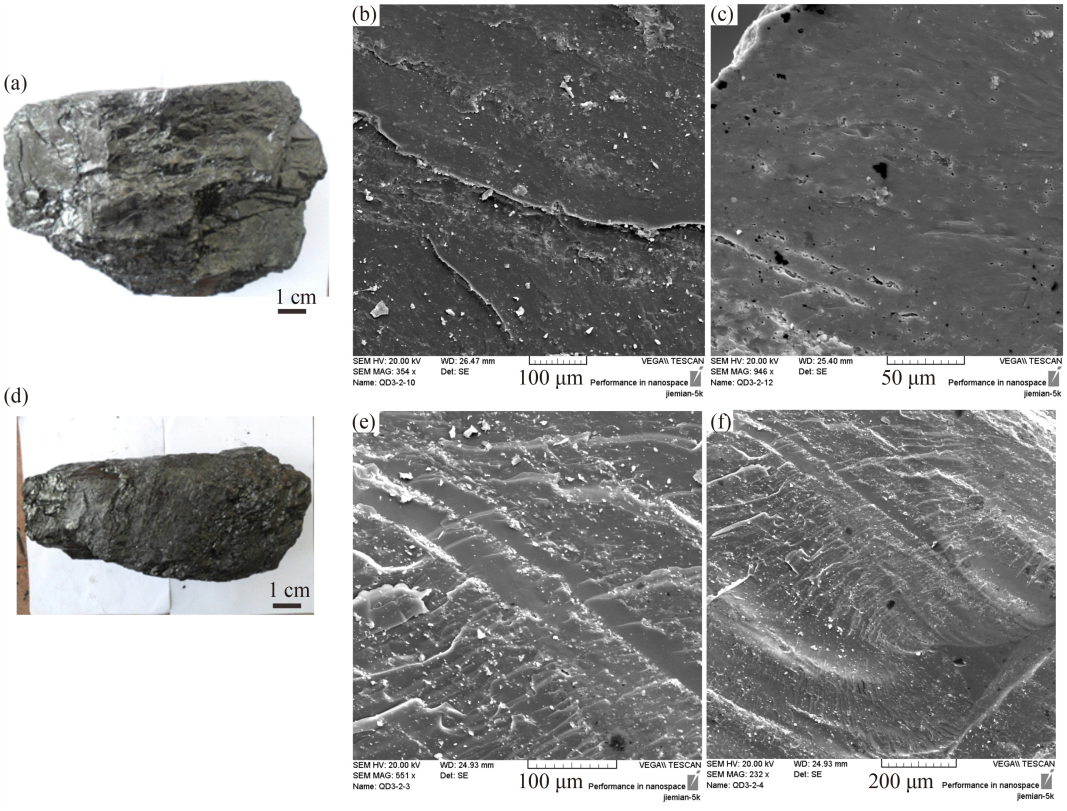

Fig. 3 Photos showing macroscopic and microscopic characteristics of undeformed coals. (a) U1; (b) and (c) SEM images showing microscopic characteristics of U1; (d) U2; (e) and (f) SEM images showing microscopic characteristics of U2.

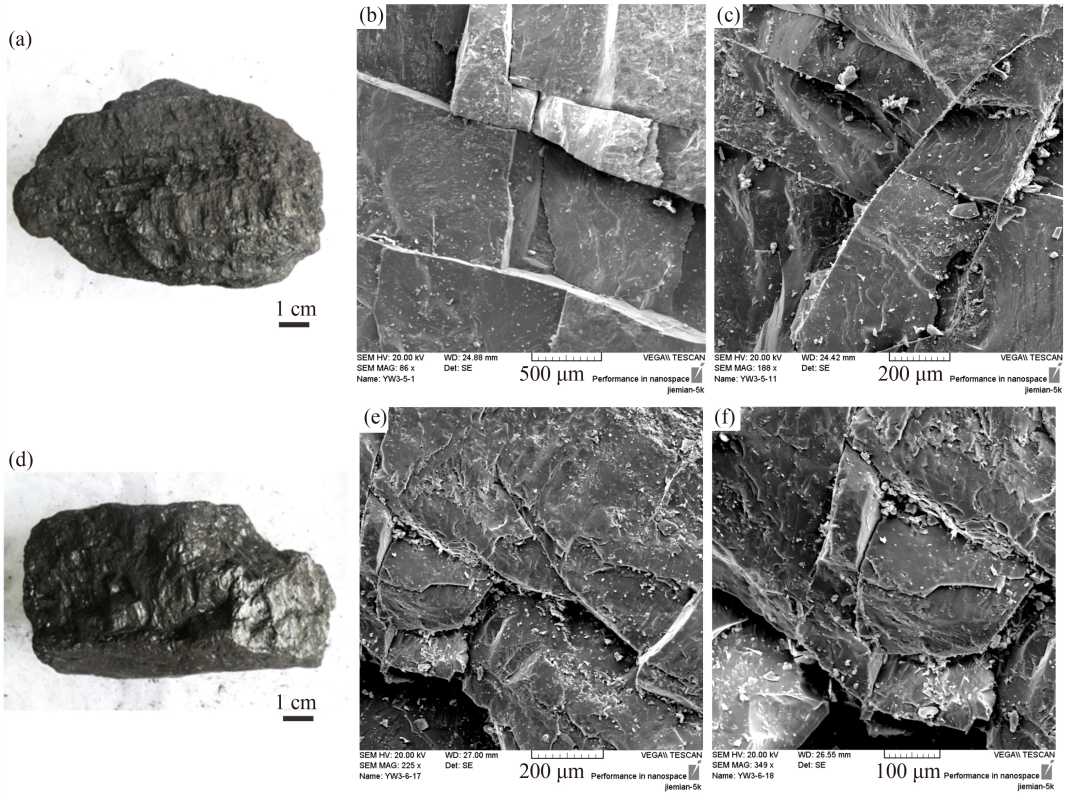

Fig. 4 Photos showing macroscopic and microscopic characteristics of cataclastic coals. (a) C1; (b) and (c) SEM images showing microscopic characteristics of C1; (d) C2; (e) and (f) SEM images showing microscopic characteristics of C2.

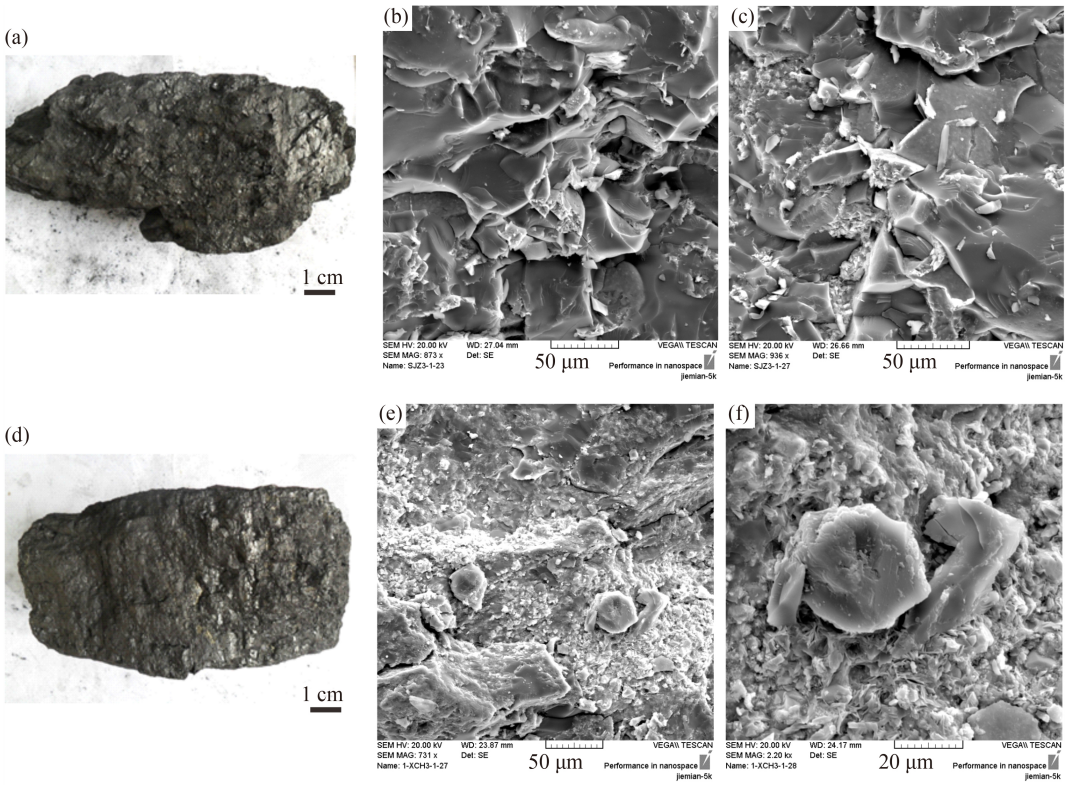

Fig. 5 Photos showing macroscopic and microscopic characteristics of cataclastic coals. (a) G1; (b) and (c) SEM images showing microscopic characteristics of G1; (d) G2; (e) and (f) SEM images showing microscopic characteristics of G2.

Table 2 Maximum vitrinite reflectance and maceral compositions of coal samples

Sample	Coal structure	$R_{o,max}$ /%	Vitrinite /vol%	Inertinite /vol%	Mineral matter /vol%
U1	Undeformed coal	3.84	88.2	11.2	0.6
C4	Cataclastic coal	2.56	70.4	28.2	1.4
G1	Granular coal	2.28	92.4	6.6	1.0

Undeformed coal samples U1 and U2 are composed of stripped clarain and durain with conchoidal fracture, which were preserved relatively intact and show metallic luster (Figs. 3(a) and 3(d)). Under SEM, undeformed coals are mainly composed of primary pores, and no obvious signs of structural transformation are shown (Figs. 3(b), 3(c), 3(e), and 3(f)).

Cataclastic coal samples of C1 and C2 are composed of stripped clarain and durain with stepped fracture, which were preserved relatively intact (Figs. 4(a) and 4(d)). Face cleat, bull cleat and natural fractures are well developed. Under SEM, cataclastic coal samples are mainly composed of primary pores and fractures, and show obvious signs of structural transformation (Figs. 4(b), 4(c), 4(e) and 4(f)).

Granular coal samples of G1 and G2 are composed of durain with stepped fracture, which have relatively low mechanical strength and hardness (Figs. 5(a) and 5(d)). Face cleat, bull cleat and natural fractures are well developed. Under SEM, granular coal samples show granulated particles (Figs. 5(b), 5(c), 5(e), and 5(f)).

4.2 Pore characteristics

Three anthracite samples with different textures were analyzed for pore size distribution (Figs. 6 and 7; Table 3). Mesopore size distribution are analyzed by N_2 adsorption isotherms and correspond to the type IV isotherm of Brunauer et al. (1938). Cataclastic coal has the largest N_2 adsorption volume of 16.8 cm^3/g. In comparison, undeformed coal shows medium N_2 adsorption volume of 10.4 cm^3/g, and granular coal has the lowest adsorption volume of 2.3 cm^3/g (Fig. 6(a)). Calculated incremental mesopore volume of the anthracite samples shows "U" shape with increasing pore width (Fig. 6(b)). A phenomenon of misclosure of adsorption and desorption branches is noticed in Fig. 6(b) for samples of undeformed and cataclastic coals. Existence of inkbottle shaped pore in high grade coals is not conducive to gas desorption, which could result in the wide distance of these two branches. Cataclastic coal has the highest BET surface area and BJH mesopore volume, undeformed coal has the medium value, and granular coal shows the lowest surface area and mesopore volume. For mesopore width, granular coal has the highest pore width, and undeformed and cataclastic coal has a similar mesopore width (Table 3).

Micropore size distribution is derived from CO_2 adsorption. Undeformed coal shows the highest CO_2

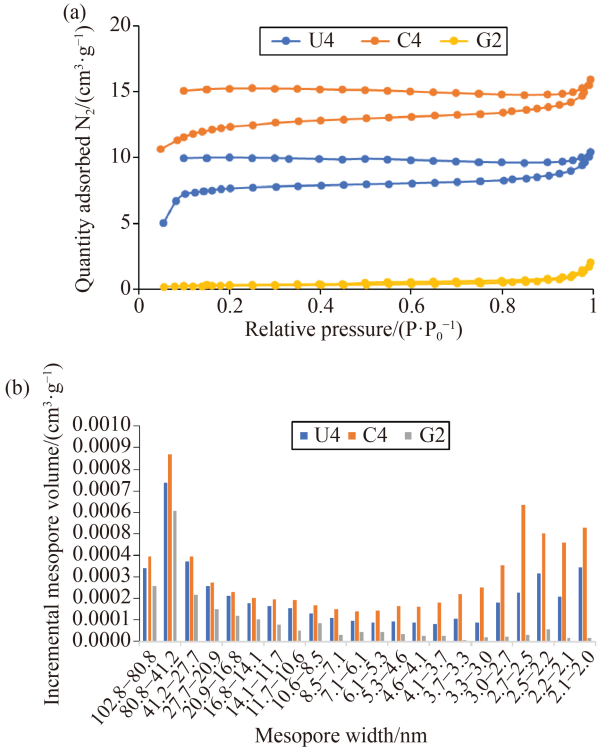

Fig. 6 Mesopore information of coal structures obtained by N_2 adsorption at low temperature. (a) N_2 adsorption capacity (P the actual gas pressure; P_0 saturated vapor pressure of adsorbed gas); (b) incremental mesopore volume. The lower branches of each sample suggest adsorption and the higher ones refer to desorption.

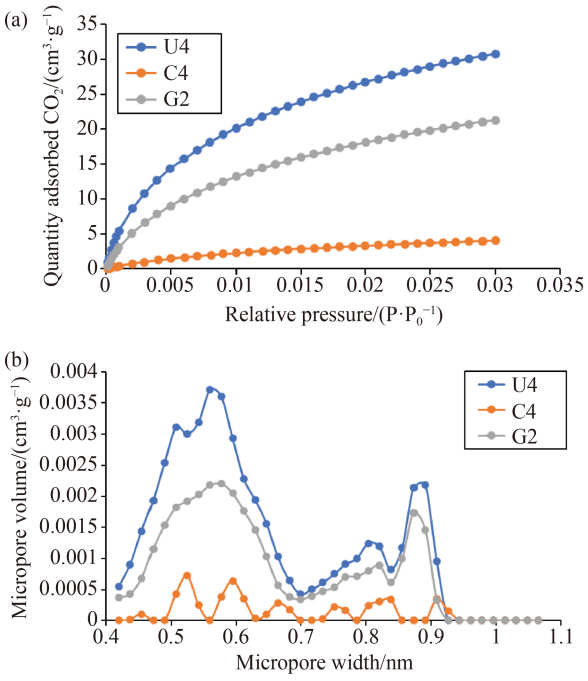

Fig. 7 Micropore information of coal structures obtained by CO_2 adsorption at low pressure. (a) CO_2 adsorption capacity (P the actual gas pressure; P_0 saturated vapor pressure of adsorbed gas); (b) micropore volume.

adsorption volume of 32.1 cm^3/g. In comparison, granular coal shows medium CO_2 adsorption volume of 22.4 cm^3/g, and cataclastic coal has the lowest adsorption volume of less than 5 cm^3/g (Fig. 7(a)). Calculated micropore volume of the anthracite samples shows relatively large micropore volume at pore with of 0.55 nm and 0.9 nm (Fig. 7(b)). Undeformed coal has the highest BET and D-R surface area, D-A micropore volume and average micropore width, and granular coal has the medium value, and cataclastic coal shows the lowest surface area, micropore volume, and width (Table 3).

4.3 Rock mechanical characteristics under uniaxial compression

Compression test is currently an important way to analyze the mechanical properties of coal and rock samples (Gonzatti et al., 2014; Poulsen et al., 2014; Li et al., 2015a). In this study, servo system records the stress and strain with loading time of anthracite with various structures (Fig. 8). From undeformed, cataclastic coal to granular coal, compression time decreases from 694 s, 558 s to 186 s, and calculated compression strength (stress divided by section area of cylinder) decreases from 14.3 MPa, 11.8 MPa to 4.2 MPa. Cataclastic coal has the largest strain of 2.8%, followed by undeformed coal of 1.9%, and granular coal has the lowest strain of 1.2%.

Stress-strain curves of anthracite with various structures were achieved according to stress and strain changes with compression time (Fig. 9). Undeformed coal underwent a short linear deformation stage (strain of 0%–0.5%) and a relatively long ductile deformation stage with strain from 0.5% to 1.2%. Cataclastic coal underwent a long linear deformation stage (strain <1.0%), and a short ductile deformation stage with strain from 1.0% to 1.1%.

Table 3 Meso- and micropore characteristics of undeformed, cataclastic and granular coals

Sample	N_2 adsorption				CO_2 adsorption			
	BET surface area /(m^2·g^{-1})	BJH surface area /(m^2·g^{-1})	BJH volume of mesopores /(cm^3·g^{-1})	Average mesopore width /nm	BET surface area /(m^2·g^{-1})	D-R micropore surface area /(m^2·g^{-1})	D-A micropore volume /(cm^3·g^{-1})	Average micropore width /nm
U4	26.3	14.3	0.0107	3.01	159.3	258.9	0.101	1.417
C4	40.8	15.2	0.0125	3.30	27.1	43.0	0.015	1.091
G2	1.0	0.9	0.0032	13.79	116.0	190.2	0.076	1.347

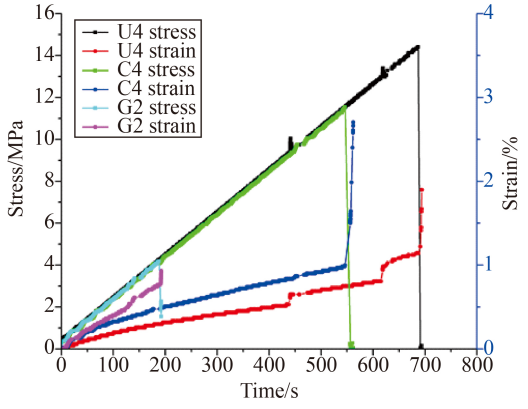

Fig. 8 Stress and strain with loading time of anthracite of various structures.

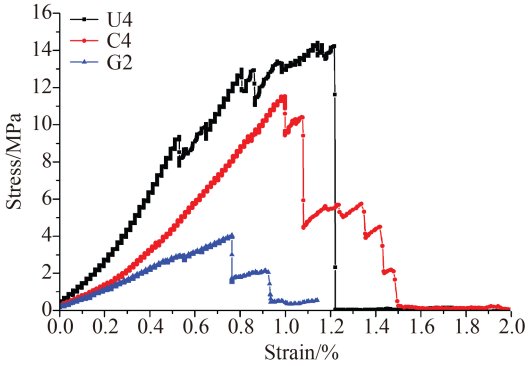

Fig. 9 Stress-strain curves of coal samples of various structures under uniaxial compression.

Granular coal only shows linear deformation, with no obvious ductile deformation. After the coal samples were broken, stress of undeformed coal drops sharply to 0, while that of cataclastic and granular coals drops step by step, and finally changes to 0.

Compression strength was achieved by the maximum stress before samples were broken, and the Young's modulus was calculated by the slope of the initial straight line of stress-strain curve (Cargill and Shakoor, 1990). Comparison of anthracite with three textures shows that from undeformed to granular coal, Young's modulus decreases from 21.2 MPa, 13.9 MPa to 5.8 MPa (Fig. 10(a)), and compression strength also shows a decreasing trend from 14.4 MPa, 11.5 MPa to 4.2 MPa (Fig. 10(b)).

Anthracite of various structures were saturated with water to analyze the rock mechanical characteristics of coals under water-saturated conditions. Sample information of weight, density and their changes after water saturation is shown in Table 4. Cataclastic coal has the highest weight change (2.04%), and granular coal has the lowest weight change (0.68%) after water saturation. The rock mechanical characteristics of coal samples change after water saturation. The Young's modulus decreases by 13%, 25% and 31% for undeformed, cataclastic, and granular coals, respectively (Fig. 10(a)), whereas the compression strength increases by 14%, 7%, and 26% for undeformed, cataclastic, and granular coals after water saturation, respectively (Fig. 10(b)).

4.4 Acoustic emission under uniaxial compression

In this study, AE characteristics of anthracite of various structures were analyzed under uniaxial compression (Fig. 11). For undeformed coal, AE counting increases with increasing strain, with local jumps or sudden increases (Fig. 11(a)). With the increasing of strain, stress dropping corresponds to sudden increases of AE counting, which indicates the formation of large fractures and release of energy. Three AE counting peaks were detected: the first two peaks were caused by newly formed fractures and the last one resulted from connection of existing fractures and complete rupture of the sample. Cataclastic coal also shows an increasing trend of AE counting with increasing strain, with a couple of sudden increases (Fig. 11(b)). During compression, AE counting peaks do not correspond to stress drops, which

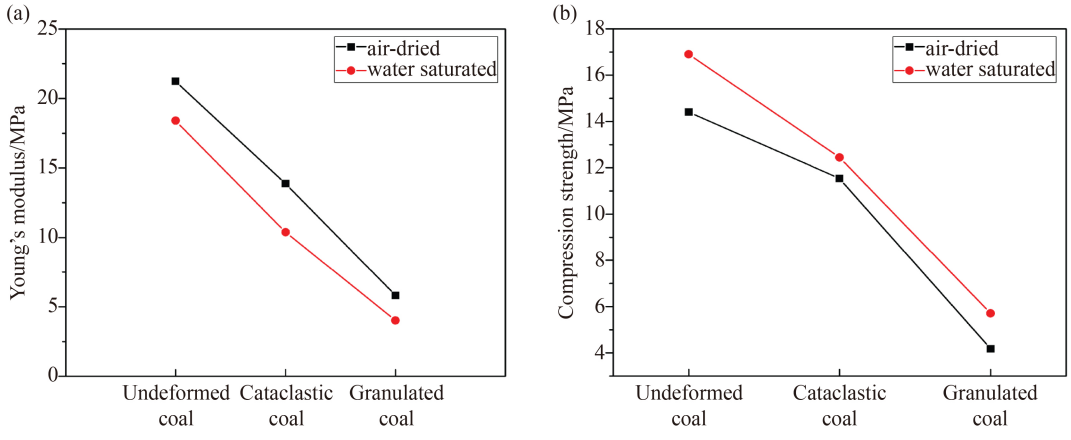

Fig. 10 Young's Modulus (a) and compression strength (b) of coal samples of various structures in dry and water-saturated conditions.

Table 4 Sample information of dry and water-saturated coal samples of various structures subject to uniaxial compression test

Sample	Diameter/cm	Height/cm	Air-dried		Water-saturated		Changes after water saturation			
							Weight		Density	
			Weight/g	Density /(g·cm^{-3})	Weight/g	Density /(g·cm^{-3})	Absolute value/g	Percentage /%	Absolute value /(g·cm^{-3})	Percentage /%
U4	2.50	5.06	37.98	1.53	38.62	1.56	0.64	1.69	0.03	1.96
C4	2.50	4.95	36.20	1.49	36.94	1.52	0.74	2.04	0.03	2.01
G2	2.50	5.02	35.24	1.43	35.48	1.44	0.24	0.68	0.01	0.70

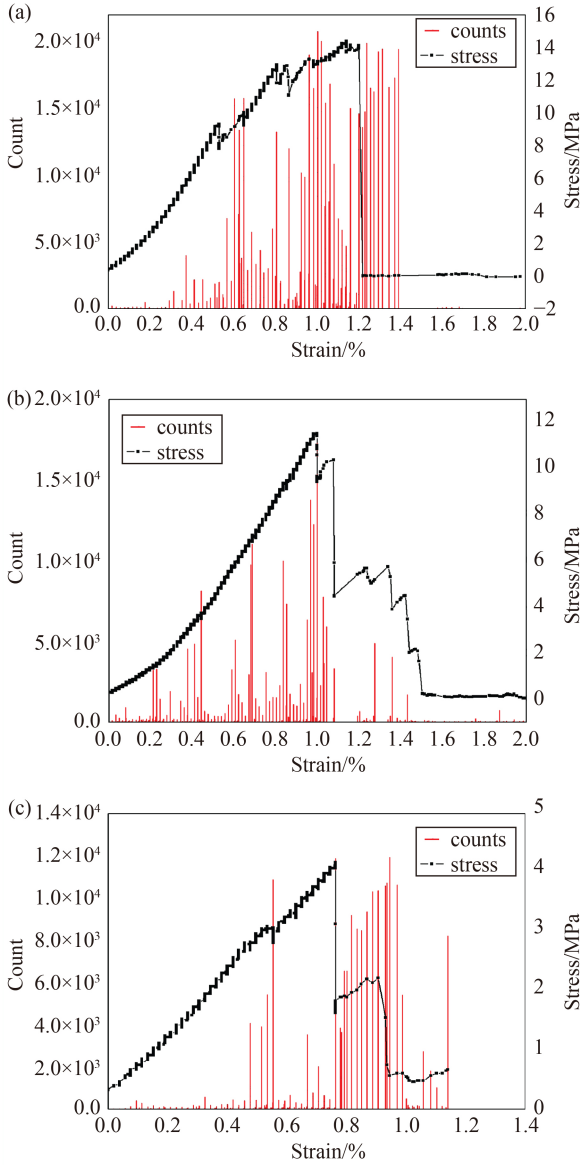

Fig. 11 Variations of acoustic emission count and stress with increasing strain of coal samples of various structures under uniaxial compression. (a) Undeformed coal, sample U4; (b) cataclastic coal, sample C4; (c) granular coal, sample G2.

indicates that the AE energy release is due to extension of pre-existing fractures instead of newly formed fractures. After cataclastic coal reached the maximum stress, the stress dropped step by step with increasing strain, which indicates that a large number of fractures were formed, and the sample was gradually fractured until it was completely broken. Compared to undeformed and cataclastic coals, granular coal shows low AE counting numbers (Fig. 11(c)). During uniaxial compression, AE counting peak corresponds to sudden drop of stress, which indicates formation of new fractures. Stress dropped step by step with increasing strain after granular coal reached the maximum stress, and the AE counting reached the highest reading, which suggests that a large number of fractures were formed after the sample was unstable, and that the sample was gradually broken until it was completely crushed.

4.5 Electrical resistivity under uniaxial compression

Electrical resistivity of anthracite of various structures were analyzed under uniaxial compression condition (Fig. 12). Resistivity of undeformed coal was about 3.2×10^4 Ω before compression, and decreased with increasing loading. It decreased to about 2.0×10^4 Ω at compression time of about 100 s, and remained stable during compression time of 100 to 600 s with resistivity value ranging from 2.0×10^4 Ω to 2.3×10^4 Ω. Before the undeformed coal was completely ruptured, the resistivity increased sharply to 6.5×10^4 Ω (Fig. 12(a)). Cataclastic coal has an original resistivity of 1.0×10^5 Ω, which is about three times higher than that of undeformed coal. During uniaxial compression, resistivity decreased to 3.5×10^4 Ω in the first 12 s of compression time. With increasing loading, resistivity increased to 1.8×10^5 Ω, then fluctuated between 0.65×10^4 and 1.2×10^5 Ω when loading time reached 72–373 s, and decreased to 3.2×10^4 to 5.0×10^4 Ω before the cataclastic coal was completely broken (Fig. 12(b)). Granular coal has the largest resistivity of 1.0×10^6 Ω before compression. During uniaxial compression, resistivity decreased at the first 15 s of compression time, and remained relatively stable between 0.5×10^6 to 1.0×10^6 Ω, but with a couple of low amplitudes. It increased to about 1.0×10^6 Ω before the granular coal was totally crushed (Fig. 12(c)).

In this study, a set of samples with water saturation was conducted for comparison with anthracite of various

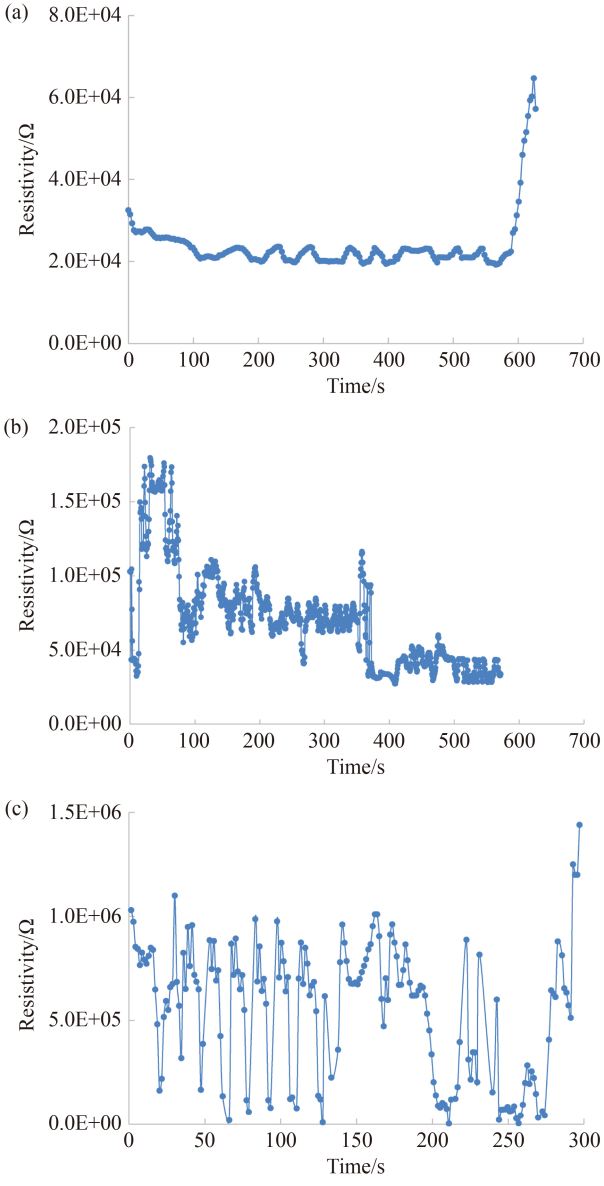

Fig. 12 Resistivity of anthracite of various textures during uniaxial compression in air dry condition. (a) Undeformed coal, sample U3; (b) cataclastic coal, sample C2; (c) granular coal, sample G2.

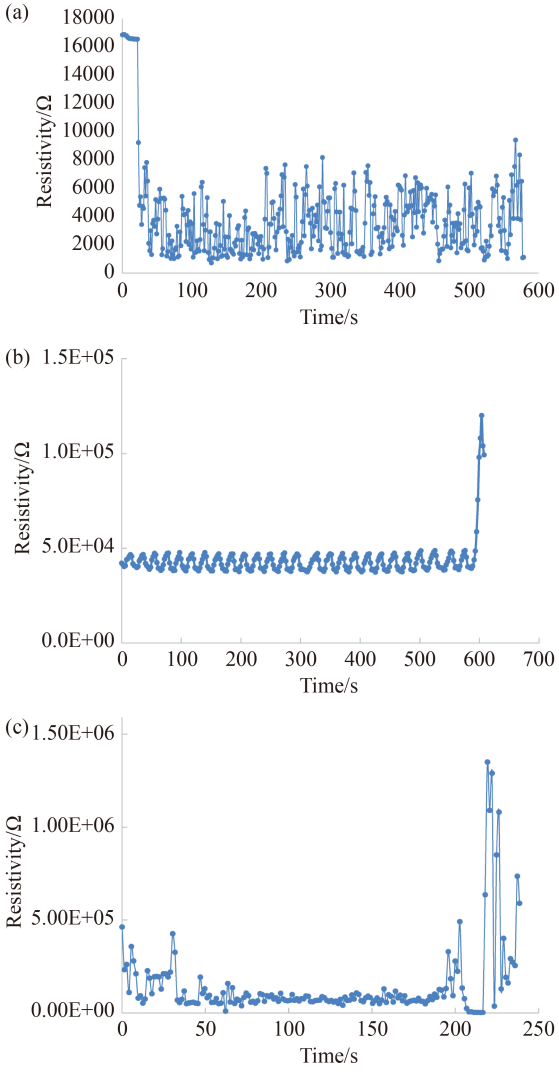

Fig. 13 Resistivity of anthracite of various structures during uniaxial compression under water-saturated condition. (a) Undeformed coal, sample U3; (b) cataclastic coal, sample C2; (c) granular coal, sample G4.

structures at dry and water-saturated conditions (Fig. 13). For undeformed coal, water-saturated sample has a resistivity value of 1.7×10^4 Ω, which is about 47% of air-dried undeformed coal. During compression, resistivity of water-saturated undeformed coal decreased to 1.0×10^3 to 8.0×10^3 Ω (Fig. 13(a)). Water-saturated cataclastic coal has a resistivity value of 4.0×10^4 Ω, which is 60% lower than that of air-dried sample. During uniaxial compression, resistivity fluctuated between 4.0×10^4 Ω and 5.0×10^4 Ω (Fig. 13(b)). Granular coal has a resistivity value of about 4.8×10^5 Ω after water saturation, which is about 66% lower than that in air-dried condition. During stress loading, resistivity fluctuated between 4.9×10^4 Ω and 1.9×10^5 Ω, and increased to 1.4×10^6 Ω before sample was completely broken (Fig. 13(c)).

4.6 Acoustic velocity under triaxial compression

Acoustic velocity of anthracite of three structures was tested under triaxial compression. P and S wave velocity during compression were recorded (Table 5 and Fig. 14). For undeformed coal, before triaxial compression, P wave velocity is 2806 m/s, and S wave velocity is 1395 m/s, which is about 49.7% of the former one. With increasing strain, S/P decreased to 47.9% at a strain of 1.0% and then increased to 48.5% at strain of 1.5% (Table 5). During compression, P wave velocity increased with increasing strain, which reached a maximum of 2924 m/s at a strain of 1.0%, and decreased to 2868 m/s at a strain of 1.5% (Fig. 14(a)). S wave velocity shows similar trends with increasing strain during compression but has lower amplitudes (Fig. 14(b)). Compared to undeformed coal, cataclastic coal has lower P and S wave velocity, but

Table 5 P and S wave velocity of anthracite of various textures during triaxial compression

Strain/%	U2			C3			G2		
	P wave /(m·s^{-1})	S wave /(m·s^{-1})	S wave/P wave × 100/%	P wave /(m·s^{-1})	S wave /(m·s^{-1})	S wave/P wave× 100/%	P wave /(m·s^{-1})	S wave /(m·s^{-1})	S wave/P wave× 100/%
0.0	2806	1395	49.7	2698	1367	50.7	2544	1289	50.7
0.5	2876	1398	48.6	2712	1372	50.6	2602	1308	50.3
1.0	2924	1402	47.9	2726	1320	48.4	2628	1299	49.4
1.5	2868	1391	48.5	2758	1365	49.5	2669	1312	49.2
2.0				2777	1337	48.1	2587	1305	50.4
2.5				2763	1333	48.2	2573	1294	50.3
3.0				2415	1212	50.2			

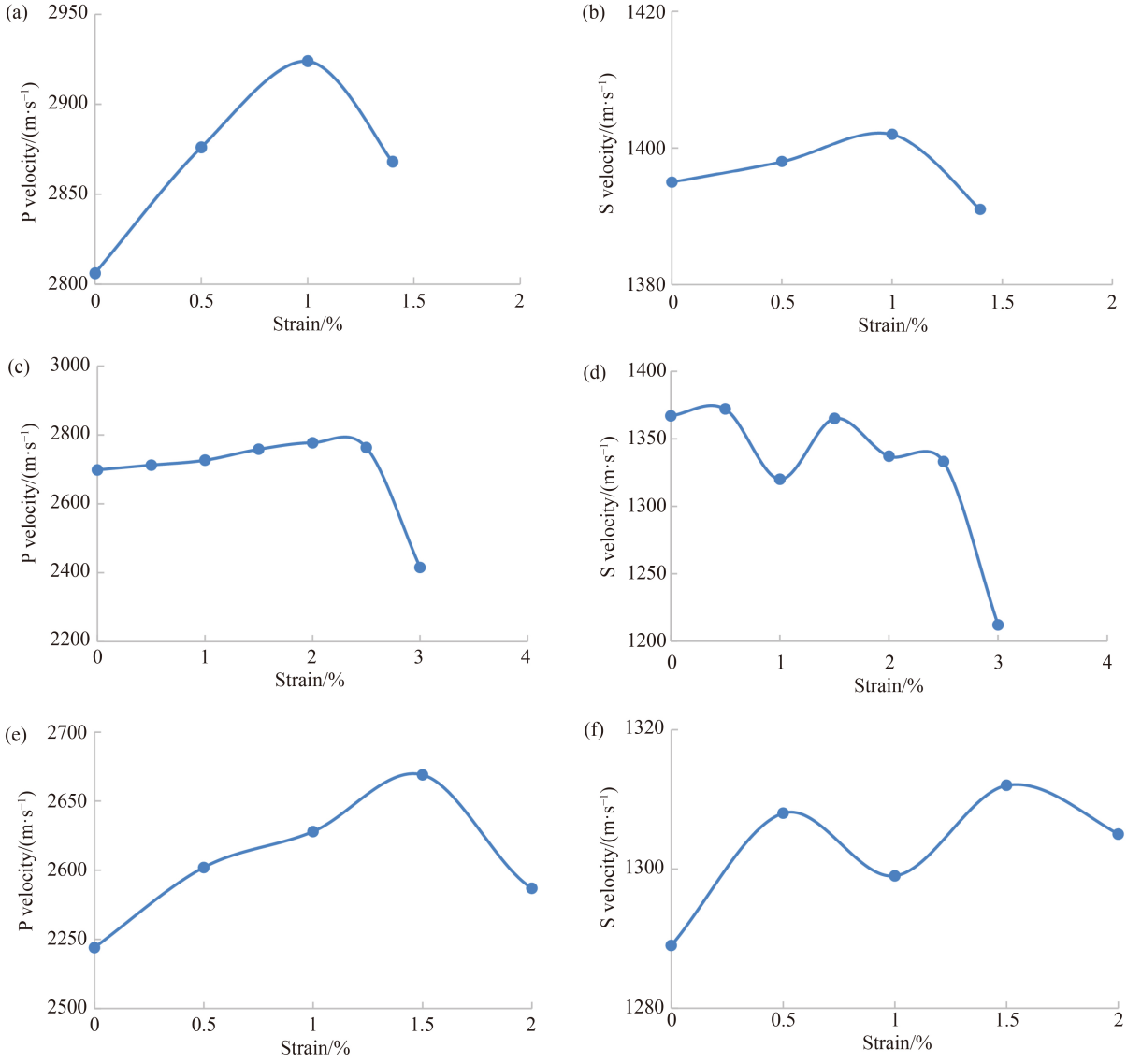

Fig. 14 P and S wave velocity of anthracite of various textures during triaxial compression. (a) and (b) Undeformed coal, sample U2; (c) and (d) cataclastic coal, sample C1; (e) and (f) granular coal, sample G2.

higher S/P value up to 50.7% (Table 5). During triaxial compression, P wave velocity increased slightly, reaching a maximum of 2763 m/s at a strain of 2.5%, and dropped sharply to 2415 m/s before the sample was completely broken (Fig. 14(c)). S wave velocity decreased slightly with increasing strain, and decreased to 1212 m/s at the

end of compression (Fig. 14(d)). Compared to undeformed and cataclastic coal, granular coal has the lowest original P (2544 m/s) and S wave velocity (1289 m/s) (Table 5). P wave velocity shows similar trends with increasing strain, with an initial increase and then decrease (Fig. 14(e)), while S wave velocity fluctuated during triaxial compression test (Fig. 14(f)).

5 Discussion

5.1 Petrographic characteristics and porosimetry

Under SEM, undeformed coal mainly develops primary pores (Figs. 3(b), 3(c), 3(e) and 3(f)). In comparison, cataclastic coal exhibits well-developed natural fractures (Fig. 4(b), 4(c), 4(e), and 4(f)), and granular coal shows mylonitic textures (Figs. 5(b), 5(c), 5(e), and 5(f)). Compared to undeformed and granular coal, cataclastic coal has the highest mesopore volume but the lowest micropore volume (Fig. 6 and Table 4), which might result from transformation of micropores to mesopores and fractures. Granular coal has the lowest mesopore volume but the highest mesopore width (Table 4), suggesting that mesopore number is much less than undeformed and cataclastic coal. Granular coal has the lowest mesopore volume but medium micropore volume (Fig. 7 and Table 4), which might result from compaction and mechanical damage. Therefore, a hypothetical pore evolution with increasing degree of damage of anthracites was proposed in this study. Before the anthracites were altered by tectonic deformation, the undeformed coal mainly has primary micropores. Under tectonic movement, undeformed coal transformed to cataclastic coal, followed by the development of fractures and transformation of micropores to mesopores. When anthracites were further altered to granular coals, mesopore number and volume decreases sharply, resulting granular structures. Maceral compositions might also contribute to pore size distribution of anthracites, of which vitrinite has a negative relationship with porosity and inertinite has positive correlations with porosity (Teng et al., 2017). Cataclastic coal has the largest inertinite content and the lowest vitrinite value (Table 2), as well as the largest porosity, which suggests that maceral compositions of cataclastic coal also make a contribution to porosity.

5.2 Geophysical characteristics during compression tests

5.2.1 Rock mechanical characteristics

Rock mechanical characteristics of anthracites were analyzed by uniaxial compression tests (Figs. 8–10). During uniaxial compression tests, stress of undeformed coal shows an approximate linear relationship with time with a couple of sudden increases of strain (Fig. 8), which might indicate that relatively large fractures were produced. After samples were broken, stress of cataclastic and granular coals decreased step by step with increasing strain (Fig. 9), which suggests that a large number of fractures might have developed at this stage. Water saturation of anthracites results in the decrease of elastic deformability, of which cataclastic coal has the most decrease of elastic deformability, and undeformed coal has the lowest value (Fig. 10(a)). For compression strength, anthracites with water saturation have larger values (Fig. 10(b)), which might be because adsorption of water improves pore pressure. Cataclastic coal has the largest water adsorption (Table 5), with the largest decrease of Young's modulus and the least increase of compression strength (Fig. 10), which suggests that water has significant effect on elastic deformability but less effect on compression strength.

5.2.2 Acoustic emission characteristics

The sharp increases of AE counting number correspond to sudden decrease of stress with increasing strain, suggesting new formation of fractures during compression tests and release of energy (Fig. 11). Undeformed coal underwent nearly linear elastic deformation, and primary pores were closed at this stage. With increasing strain, a couple of new fractures were formed before the sample was completely broken (Fig. 11(a)). Results obtained from AE counting and stress with increasing strain show that undeformed coal consists mainly of primary pores, with no pre-existing fractures, which is consistent with SEM observations (Figs. 3(b), 3(c), 3(e), and 3(f)). Cataclastic coal has a relatively longer process of plastic deformation (Fig. 11(b)), suggesting the closure of pre-existing fractures, which shows a good consistency with SEM observations with well-developed fractures (Figs. 4(b), 4(c), 4(e), and 4(f)). Granular coal does not show many pre-existing fractures (Fig. 11(c)), which agrees with SEM observations (Figs. 5(b), 5(c), 5(e), and 5(f)).

5.2.3 Electrical resistivity characteristics

Changes of electrical resistivity of anthracites during compression tests reflect electric conductivity of coal particles and pores. For undeformed coal, resistivity decreased at the first 50 s of compression time (Fig. 12(a)), which might result from closure of primary pores and increasing electric conductivity. Fluctuation of resistivity during compression test might indicate closure of pores and fractures and newly formed pores and fractures. Cataclastic coal has high resistivity value at the first stage (Fig. 12(b)), which could be the result of extension of pre-existing fractures. Closure of fractures might result in decrease of resistivity of cataclastic coal. For granular coal, resistivity increased sharply at the end of

compression test (Fig. 12(c)), indicating that a large number of fractures were produced until the sample was completely broken. Comparison of undeformed, cataclastic and granular coals before compression shows that resistivity increases with increasing degree of damage, and that the resistivity of cataclastic coal is 30 times higher than that of undeformed coal, which agrees with previous study (Lv and He, 2000). Water decreases resistivity of anthracites and makes the value uniform during compression. We suggest that water adsorbed in pores and fractures increases electrical conductivity. Granular coal is mainly controlled by micropores (Table 4), which has the largest decrease of resistivity after saturation of about 66%, suggesting that water has significant effect on the resistivity of samples consisting of mainly micropores.

5.2.4 Acoustic velocity characteristics

P and S wave velocity of anthracites of three structures shows sharp decreases at the end of compression tests (Fig. 14), suggesting a large number of pore and fracture formation, which agrees with results from AE and resistivity during uniaxial compression (Figs. 11 and 12). With increasing degree of damage, from undeformed to granular coal, P and S wave velocity decreases (Fig. 14), suggesting that more pore volume was produced. Compared to undeformed coal, P and S wave velocity of cataclastic coal appears more complicated (Fig. 14(c) and 14(d)), likely because pre-existing fractures improves the heterogeneity of the sample. P and S wave velocity of granular coal also shows no univocal change (Figs. 14(e) and 14(f)), which might result from characteristics of granular particles and the microporous nature.

6 Conclusions

Petrographic observations, pore size distribution, and geophysical characteristics of anthracites of three types of structures in the Qinshui Basin, north China were investigated in this study, based on which we proposed evolutionary pathways of pore structure during deformation of anthracites from undeformed to granular structure and dynamic evolution of geophysical parameters during uniaxial/triaxial compression tests. Specific conclusions are as follows.

1) A hypothetical pore evolution with increasing damage degree of anthracites was proposed. Undeformed coal mainly contains primary micropores. Under tectonic movement, undeformed coal transforms to cataclastic coal, resulting in the development of fractures and transformation of micropores to mesopores. When anthracites are transformed to granular coals, granular structure forms, and mesopore number and volume decreases sharply.

2) Geophysical characteristics of anthracites exhibit significant changes with increasing alteration degree: compression strength, Young's modulus, density, AE counting, and acoustic velocity decrease, and resistivity increases with pressure loading. Evolution of pore size distribution and fracture closure and formation of anthracites with increasing damage degree might control the geophysical characteristics of anthracites of three types of coal structures.

Acknowledgments This research was supported by the National Natural Science Foundation of China (Grant No. 42102194).

References

Bieniawski Z T (1968). *In situ* strength and deformation characteristics of coal. Eng Geol, 2(5): 325–340

Brunauer S, Emmett P H, Teller E (1938). Adsorption of gases in multimolecular layers. J Am Chem Soc, 60(2): 309–319

Cai Y D, Liu D M, Yao Y B, Li J Q, Qiu Y K (2011). Geological controls on prediction of coalbed methane of No. 3 coal seam in Southern Qinshui Basin, north China. Int J Coal Geol, 88(2): 101–112

Cargill J S, Shakoor A (1990). Evaluation of empirical methods for measuring the uniaxial compressive strength of rock. Int J Rock Mech Min Sci Geomech Abstr, 27(6): 495–503

Chen F Y, Ju Y W, Li X S, Fan J J, Liang Y (2010). Diffusion-seepage characteristics and mechanism of coalbed methane in tectonic coal. Earth Sci Front, 1: 195–201 (in Chinese)

Chen H D, Jiang B, Chen T J, Xu S C, Zhu G Y (2017). Experimental study on ultrasonic velocity and anisotropy of tectonically deformed coal. Int J Coal Geol, 179: 242–252

Chen S D, Tao S, Tian W G, Tang D Z, Zhang B, Liu P C (2021). Hydrogeological control on the accumulation and production of coalbed methane in the Anze Block, southern Qinshui Basin, China. J Petrol Sci Eng, 198: 108138

Cheng Y P, Pan Z J (2020). Reservoir properties of Chinese tectonic coal: a review. Fuel, 260: 116350

Clarkson C R, Bustin R M (1999). The effect of pore structure and gas pressure upon the transport properties of coal: a laboratory and modeling study: 1. Isotherms and pore volume distributions. Fuel, 78(11): 1333–1344

Deisman N, Ivars D M, Darcel C, Chalaturnyk R J. (2010). Empirical and numerical approaches for geomechanical characterization of coal seam reservoirs. Int J Coal Geol, 82(3–4): 204–212

Frodsham K, Gayer R A. (1999). The impact of tectonic deformation upon coal seams in the South Wales coalfield, UK. Int J Coal Geol, 38(3–4): 297–332

Fu X H, Qin Y, Wang G G, Rudolph V (2009). Evaluation of coal structure and permeability with the aid of geophysical logging technology. Fuel, 88(11): 2278–2285

Geng Z, Chen M, Jin Y, Yang S, Yi Z C, Fang X, Du X Y (2016). Experimental study of brittleness anisotropy of shale in triaxial compression. J Nat Gas Sci Eng, 36: 510–518

Godyń K (2016). Structurally altered hard coal in the areas of tectonic

disturbances——an initial attempt at classification. Arch Min Sci, 61(3): 677–694

Gonzatti C, Zorzi L, Agostini I M, Fiorentini J A, Viero A P, Philipp R P (2014). In situ strength of coal bed based on the size effect study on the uniaxial compressive strength. Int J Min Sci Technol, 24(6): 747–754

Guo H J, Wang K, Wu Y C, Tang H L, Wu J G, Guan L H, Chang C Y, Xu C (2021). Evaluation of the weakening behavior of gas on the coal strength and its quantitative influence on the coal deformation. Int J Min Sci Technol, 31(3): 451–462

International Committee for Coal Petrology (ICCP) (1963). International Handbook of Coal Petrography. 2ed. The National Center for Scientific Research. Academy of Sciences of the USSR, Moscow

Jiang B, Qu Z H, Wang G G, Li M. (2010). Effects of structural deformation on formation of coalbed methane reservoirs in Huaibei coalfield, China. Int J Coal Geol, 82(3–4): 175–183

Jin X L, Li J W, Yang Z Y, Zhang P H (2011). The optimization of the coalbed methane assessment indexes in the high abundance coalbed methane enrichment area in the case of the southern part of the Qinshui Basin, China. Procedia Earth and Planetary Science, 3: 175–182

Li L J, Liu D M, Cai Y D, Wang Y J, Jia Q F (2021a). Coal structure and its implications for coalbed methane exploitation: a review. Energy Fuels, 35(1): 86–110

Li M, Jiang B, Lin S F, Wang J L, Ji M J, Qu Z H (2011). Tectonically deformed coal types and pore structures in Puhe and Shanchahe coal mines in western Guizhou. Mining Sci Techn (China), 21(3): 353–357

Li S, Tang D, Pan Z J, Xu H, Huang W Q (2013). Characterization of the stress sensitivity of pores for different rank coals by nuclear magnetic resonance. Fuel, 111: 746–754

Li W F, Bai J B, Cheng J Y, Peng S, Liu H L (2015a). Determination of coal–rock interface strength by laboratory direct shear tests under constant normal load. Int J Rock Mech Min Sci, 77: 60–67

Li W, Liu H F, Song X X (2015b). Multifractal analysis of Hg pore size distributions of tectonically deformed coals. Int J Coal Geol, 144: 138–152

Li X S, Yin G Z, Zhao H B, Wang W Z, Jing X F (2010). Experimental study on mechanical properties of coal with gas outburst under triaxial Compression. In: Proceedings of the 11th National Conference on Rock Mechanics and Engineering, 29: 3350–3358

Li X, Zhang J, Li C N, Li B, Zhao H Y, Li R X, Qi Q (2021b). Variation characteristics of coal–rock mechanical properties under varying temperature conditions for Shanxi Linfen coalbed methane well in China. J Pet Explor Prod Technol, 11(7): 2905–2915

Li Z T, Liu D M, Ranjith P G, Cai Y D, Wang Y J (2018). Geological controls on variable gas concentrations: a case study of the northern Gujiao Block, northwestern Qinshui Basin, China. Mar Pet Geol, 92: 582–596

Liu B, Teng J, Mastalerz M, Schieber J, Schimmelmann A, Bish D (2021). Compositional control on shale pore structure characteristics across a maturation gradient: insights from the Devonian New Albany Shale and Marcellus Shale in the eastern United States. Energy Fuels, 35(9): 7913–7929

Liu H H, Sang S X, Wang G G, Li M X, Xu H J, Liu S Q, Li J J, Ren B, Zhao Z G, Xie Y (2014). Block scale investigation on gas content of coalbed methane reservoirs in southern Qinshui Basin with statistical model and visual map. J Petrol Sci Eng, 114: 1–14

Liu X S, Tan Y L, Ning J G, Lu Y W, Gu Q H (2018). Mechanical properties and damage constitutive model of coal in coal–rock combined body. Int J Rock Mech Min Sci, 110: 140–150

Lv S L, He J S, Li Z B (2000). Study on electrical conductivity of coal outburst under simulated reservoir condition. World Geo, 19(1): 82–86 (in Chinese)

Lv Y M, Tang D Z, Xu H, Luo H H (2012). Production characteristics and the key factors in high–rank coalbed methane fields: a case study on the Fanzhuang Block, southern Qinshui Basin, China. Int J Coal Geol, 96: 93–108

Ma Y K, Nie B S, He X Q, Li X C, Meng J Q, Song D Z (2020). Mechanism investigation on coal and gas outburst: an overview. Int J Miner Metall Mater, 27(7): 872–887

Mastalerz M, He L, Melnichenko Y B, Rupp J A (2012). Porosity of coal and shale: insights from gas adsorption and SANS/USANS techniques. Energy Fuels, 26(8): 5109–5120

Mastalerz M, Schimmelmann A, Drobniak A, Chen Y (2013). Porosity of Devonian and Mississippian New Albany Shale across a maturation gradient: insights from organic petrology, gas adsorption, and mercury intrusion. AAPG Bull, 97(10): 1621–1643

Nie B, Ma Y, Hu S, Meng J (2019). Laboratory study phenomenon of coal and gas outburst based on a mid–scale simulation system. Sci Rep, 9(1): 15005

Orr C (1977). Pore size and volume measurement. Treatise on Analytical Chemistry (Part III), 4: 321–358

Poulsen B A, Shen B, Williams D J, Huddlestone-Holmes C, Erarslan N, Qin J (2014). Strength reduction on saturation of coal and coal measures rocks with implications for coal pillar strength. Int J Rock Mech Min Sci, 71: 41–52

Qu Z H, Wang G G, Jiang B, Rudolph V, Dou X Z, Li M (2010). Experimental study on the porous structure and compressibility of tectonized coals. Energy Fuels, 24(5): 2964–2973

Skoczylas N, Dutka B, Sobczyk J (2014). Mechanical and gaseous properties of coal briquettes in terms of outburst risk. Fuel, 134: 45–52

Sobczyk J (2011). The influence of sorption processes on gas stresses leading to the coal and gas outburst in the laboratory conditions. Fuel, 90(3): 1018–1023

Su X B, Lin X Y, Liu S B, Zhao M J, Song Y (2005). Geology of coalbed methane reservoirs in the southeast Qinshui Basin of China. Int J Coal Geol, 62(4): 197–210

Tao S, Chen S D, Pan Z J (2019). Current status, challenges, and policy suggestions for coalbed methane industry development in China: a review. Energy Sci Eng, 7(9): 1059–1074

Tao S, Wang Y B, Tang D Z, Xu H, Lv Y M, He W, Li Y (2012). Dynamic variation effects of coal permeability during the coalbed methane development process in the Qinshui Basin, China. Int J Coal Geol, 93(1): 16–22

Teng J, Mastalerz M, Hampton L (2017). Maceral controls on porosity characteristics of lithotypes of Pennsylvanian high volatile bituminous coal: example from the Illinois Basin. Int J Coal Geol,

172: 80–94

Teng J, Yao Y B, Liu D M, Cai Y D (2015). Evaluation of coal texture distributions in the southern Qinshui Basin, north China: Investigation by a multiple geophysical logging method. Int J Coal Geol, 140: 9–22

Wang Y J, Liu D M, Cai Y D, Yao Y B, Zhou Y F (2018). Evaluation of structured coal evolution and distribution by geophysical logging methods in the Gujiao Block, northwest Qinshui Basin, China. J Nat Gas Sci Eng, 51: 210–222

Webb P A, Orr C (1997). Analytical Methods in Fine Particle Technology. Micromeritics Instrument Corporation, Norcross, Georgia, USA, 161–162

Wei C T, Qin Y, Wang G G, Fu X H, Jiang B, Zhang Z Q (2007). Simulation study on evolution of coalbed methane reservoir in Qinshui Basin, China. Int J Coal Geol, 72(1): 53–69

Wu C, Yuan C X, Wen G J, Han L, Liu H J (2020). A dynamic evaluation technique for assessing gas output from coal seams during commingling production within a coalbed methane well: a case study from the Qinshui Basin. Int J Coal Sci Technol, 7(1): 122–132

Xie H P, Gao M Z, Zhang R, Peng G Y, Wang W Y, Li A Q (2019). Study on the mechanical properties and mechanical response of coal mining at 1000 m or deeper. Rock Mech Rock Eng, 52(5): 1475–1490

Xu H, Tang D Z, Tang S H, Zhao Y J, Meng S T (2014). A dynamic prediction model for gas–water effective permeability based on coalbed methane production data. Int J Coal Geol, 121(1): 44–52

Xue G W, Liu H F, Li W (2012). Deformed coal types and pore characteristics in Hancheng coalmines in eastern Weibei coalfields. Int J Min Sci Technol, 22(5): 681–686

Yao Z, Cao D Y, We Y C, Li X M, Wang X L, Zhang X Y (2016). Experimental analysis on the effect of tectonically deformed coal types on fines generation characteristics. J Petrol Sci Eng, 146: 350–359

Yin G Z, Jiang C B, Wang J G, Xu J, Zhang D M, Huang G (2016). A new experimental apparatus for coal and gas outburst simulation. Rock Mech Rock Eng, 49(5): 2005–2013

Yu K, Ju Y W, Zhang B X (2020a). Modeling of tectono–thermal evolution of Permo-Carboniferous source rocks in the southern Qinshui Basin, China: consequences for hydrocarbon generation. J Petrol Sci Eng, 193: 107343

Yu S, Bo J, Ming L, Hou C L, Xu S C (2020b). A review on pore-fractures in tectonically deformed coals. Fuel, 278: 118248

Zhang H B, Liu J S, Elsworth D (2008). How sorption-induced matrix deformation affects gas flow in coal seams: a new FE model. Int J Rock Mech Min Sci, 45(8): 1226–1236

Zhang S, Zhang X D, Li G Z, Liu X, Zhang P (2019). Distribution characteristics and geochemistry mechanisms of carbon isotope of coalbed methane in central-southern Qinshui Basin, China. Fuel, 244: 1–12

Zhou Y B, Li Z H, Yang Y L, Zhang L J, Qi Q Q, Si L L, Li J H (2016). Improved porosity and permeability models with coal matrix block deformation effect. Rock Mech Rock Eng, 49(9): 3687–3697

Zou G G, Peng S P, Yin C Y, Xu Y Y, Chen F Y, Liu J K (2013). Seismic studies of coal bed methane content in the west coal mining area of Qinshui Basin. Int J Min Sci Technol, 23(6): 795–803